Journal of Biomolecular NMR **28:** 311–325, 2004.
KLUWER/ESCOM

Signal assignments and chemical-shift structural analysis of uniformly ^{13}C, ^{15}N-labeled peptide, mastoparan-X, by multidimensional solid-state NMR under magic-angle spinning

Toshimichi Fujiwara[a,*], Yasuto Todokoro[a], Hajime Yanagishita[b], Midori Tawarayama[b], Toshiyuki Kohno[c], Kaori Wakamatsu[d] & Hideo Akutsu[a]

[a]*Institute for Protein Research, Osaka University, 3-2 Yamadaoka, Suita, 565-0871 Japan;* [b]*Department of Chemistry and Biotechnology, Yokohama National University, Hodogaya, Yokohama 240-8501, Japan;* [c]*Mitsubishi Kagaku Institute of Life Sciences (MITILS), Minamiooya, Machida, Tokyo, 194-8511, Japan;* [d]*Department of Biochemical Sciences, Gunma University, Tenjin-cho, Kiryu, Gunma 376-8515, Japan*

Received 22 May 2003; Accepted 9 October 2003

Key words: isotope-labeling, magic-angle spinning, mastoparan-X, multidimensional NMR, recoupling, signal assignment, solid-state NMR

Abstract

Carbon-13 and nitrogen-15 signals of fully isotope-labeled 15-residue peptide, glycinated mastoparan-X, in a solid state were assigned by two- and three-dimensional NMR experiments under magic-angle spinning conditions. Intra-residue spin connectivities were obtained with multidimensional correlation experiments for C'–C^{α}–C^{β} and N–C^{α}–C^{β}. Sequence specific assignments were performed with inter-residue C^{α}–C^{α} and N–$C^{\alpha}C^{\beta}$ correlation experiments. Pulse sequences for these experiments have mixing periods under recoupled zero- and double-quantum ^{13}C–^{13}C and ^{15}N–^{13}C dipolar interactions. These correlation spectra allowed the complete assignments of ^{13}C and ^{15}N backbone and $^{13}C^{\beta}$ signals. Chemical shift analysis of the ^{13}C and ^{15}N signals based on empirical and quantum chemical databases for proteins indicated that the backbone between residues 3 and 14 forms α-helix and residue 2 has extended conformation in the solid state. This structure was compared with the G-protein- and membrane-bound structures of mastoparan-X.

Introduction

Multidimensional magic-angle-spinning (MAS) NMR of multiply isotope-labeled proteins and peptides can provide constraints sufficient for the structure determination, similarly to solution NMR (Nomura et al., 2000; Castellani et al., 2002; Rienstra et al., 2002). Recent developments of the solid-state NMR allow the detailed analyses of the structure and function of membrane and amyloid proteins which are difficult for X-ray crystallography and solution NMR (de Groot, 2000; Balbach et al., 2000b; Hughes et al., 2003). To obtain structural constraints from the spectra, we must first assign signals by using the intra- and inter-residue spin-connectivities acquired with a suite of solid-state NMR experiments. A number of pulse techniques developed in the past decade, such as recoupling of dipolar interactions for ^{13}C and ^{15}N, can be applied to the signal assignments and structural analysis of uniformly isotope-labeled biomolecules (Griffin, 1998; Detken et al., 2001; Baldus, 2002).

Several ^{13}C–^{13}C and ^{13}C–^{15}N correlation experiments under MAS conditions have been carried out for sequential signal assignments of uniformly isotope-labeled biomolecules (Fujiwara et al., 1995; Rienstra et al., 2000). Partial assignments of the signals were reported for small proteins (Straus et al., 1998; Hong 1999; McDermott et al., 2000; Egorova-Zachernyuk et al., 2001). Polycrystalline samples can have ^{13}C linewidths of about 0.5 ppm at higher static fields

*To whom correspondence should be addressed. E-mail: tfjwr@protein.osaka-u.ac.jp

(Pauli et al., 2000, 2001). Such high spectral resolution allowed almost complete ^{13}C and ^{15}N signal assignments of a 63-residue protein. At lower B_0 fields, dilution of ^{13}C spin may be preferable for the assignment to reduce the linewidth due to ^{13}C homonuclear spin couplings (LeMaster and Kushlan, 1996; Hong and Jakes, 1999). The linewidths of carbon-13 signals of peptides in noncrystalline states are generally larger than those for crystalline states. The feasibility of the signal assignments of larger peptides depends greatly on the spectral resolution or the linewidth relative to the chemical shift dispersion. The improvement of the assignment methods is crucial for increasing the size of molecules to which the solid-state NMR is applicable (Astrof and Griffin, 2002; Petkova et al., 2003).

We have assigned most of ^{13}C,^{15}N signals of a uniformly labeled 15-residue peptide at the static field of about 10 T where typical linewidth was about 2 ppm. The present experimental results demonstrate the practical applicability of newly developed methods to medium-size peptides in solid states. The assignments were performed with two- and three-dimensional isotropic chemical shift correlation pulse sequences having mixing periods by the dipolar couplings for ^{13}C–^{13}C and ^{13}C–^{15}N along the covalent bonds. We have employed the inter-residue correlation experiments between C^{α} spins and between N and C^{β} spins for the sequence specific signal assignments. These correlation spectra have higher resolution due to the large chemical shift dispersion of C^{α} and C^{β}.

The peptide we studied is mastoparan-X (MP-X) glycinated at the C-terminus, Ile-Asn-Trp-Lys-Gly-Ile-Ala-Ala-Met-Ala-Lys-Lys-Leu-Leu-Gly. Mastoparan-X is an amphipathic peptide found in wasp venom. This peptide interacts with phospholipid membranes, and was shown to disrupt the lipid bilayers (Matsuzaki et al., 1996). Similarly to G-protein coupled receptors, MP-X activates G-proteins (Higashijima et al., 1990). Glycinated MP-X retains this biochemical function (T. Ishii and K. Wakamatsu, unpublished data). The structures of the membrane-bound form and G-protein-bound form have been determined by transferred NOE studies in solution states (Wakamatsu et al., 1992; Kusunoki et al., 1998). Mastoparan having a homologous amino acid sequence has also been studied by solution NMR (Vold et al., 1997; Lindberg et al., 2001). In the present study, MP-X precipitated from the methanol solution was analyzed with solid-state NMR. We have compared those solution and the solid-state NMR structures by using

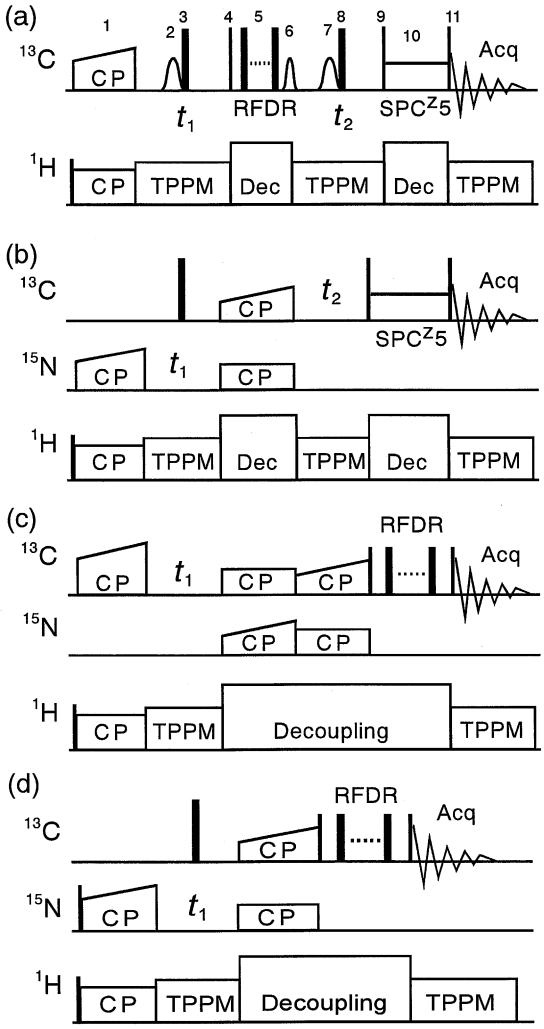

Figure 1. Pulse sequences for 3D C'_i–C^{α}_i–C^{β}_i (a), 3D N_i–C^{α}_i–C^{β}_i (b), 2D $(C^{\alpha}C^{\beta})_{i+1}$–$(C'C^{\alpha})_i$ (c), and 2D N_{i+1}–$(C'C^{\alpha}C^{\beta})_i$ correlation experiments (d) under MAS conditions. Here, the subscripts, i and i+1, indicate the residue numbers. The sequences consist of the evolution periods for ^{13}C and ^{15}N isotropic chemical shifts and the mixing periods under ^{13}C–^{13}C and ^{13}C–^{15}N dipolar couplings. The thin and thick dark pulses represent $\pi/2$ and π pulses, respectively. In (a), pulse 6 is a selective Gaussian excitation pulse for C^{α}, and pulses 2 and 7 are selective Gaussian 180° pulses applied to C' and C^{α} spins, respectively.

chemical shifts obtained with the signal assignments. Conformation dependence of ^{13}C and ^{15}N chemical shifts is well studied for proteins (Wishart and Sykes, 1994). The reliability of the predicted structure is evaluated with empirical and quantum chemical database programs for peptides and proteins.

Materials and methods

NMR experiments

Multidimensional correlation pulse sequences under MAS shown in Figure 1 were utilized for ^{13}C and ^{15}N signal assignments. The initial magnetization for the experiments was prepared by ramped-amplitude cross-polarization from the proton magnetization with a contact time of about 2.0 ms (Metz and Smith, 1994). The RF field amplitude for ^{13}C and ^{15}N, $\gamma B_{1,X}$, was varied linearly near the first sideband of the Hartmann-Hahn condition, $\gamma B_{1,X} = \gamma B_{1H} - \omega_R$, here γB_{1H} and ω_R are ^{1}H RF field amplitude and the sample spinning frequency, respectively. The ^{1}H RF field amplitude was 55 kHz and 47 kHz for double and triple resonance experiments, respectively. The ^{1}H, ^{13}C and ^{15}N RF field amplitudes for $\pi/2$ pulses were typically 70 kHz, 60 kHz and 40 kHz, respectively. The sample spinning frequency was 10.0 kHz and 12.5 kHz within a precision of about 10 Hz for experiments at static fields of 9.4 T and 11.75 T, respectively. The dwell time was 25 μs and 20 μs for the experiments at 9.4 T and 11.75 T, respectively, unless otherwise specified. The CH dipolar interactions during the evolution and mixing periods were decoupled with TPPM and CW RF fields at the amplitudes of about 72 and 97 kHz, respectively. The TPPM sequence comprised 170° pulses with RF phase shifts of 14° (Bennett et al., 1995). The relaxation delay between experiments was about 3.5 s.

Two-dimensional broadband ^{13}C–^{13}C correlation spectra were obtained with a sequence having a zero-quantum ^{13}C dipolar mixing period under an RFDR pulse sequence with the RF field amplitude of 50 kHz (Bennett et al., 1998; Fujiwara et al., 2000). A band-selective correlation experiment for the aliphatic ^{13}C region was performed with a sequence having a double-quantum (DQ) ^{13}C–^{13}C dipolar mixing period under the SPC^{z}5 pulse sequence (Matsuki et al., 2003). The element composite 0° pulse $180^\circ_x\, 180^\circ_{-x}$ was applied synchronously with the sample rotation according to the SPC5 phase modulation (Hohwy et al., 1999). The B_1 field amplitude was 25 kHz. The mixing time was 0.8 and 2.4 ms for RFDR and 1.6 ms for SPC^{z}5. The experimental data matrices $512(t_1)$x$512(t_2)$ for the RFDR mixing and $360(t_1)\times408(t_2)$ for the SPC^{z}5 mixing were zero-filled to 1024×1024. The number of transients for each FID was 32. The ^{13}C RF phases for the cross polarization and 90° pulses preceding and following the mixing period were alternated independently to select the pathway of the coherence transfer. The ^{13}C RF phases for the cross polarization were cycled following the States method for the phase-sensitive detection. Experimental time for the RFDR correlation at the mixing time of 2.4 ms was 43 h, and that for other ^{13}C–^{13}C correlations was about 20 h. The S/N ratio of the cross peak for I6 $C^\alpha C^\beta$ in the RFDR spectrum at the mixing time of 2.4 ms was 8.0, and that for other ^{13}C–^{13}C correlation experiments was about 5.

The 3D C'_i–C^α_i–C^β_i correlation experiment was performed with the pulse sequence shown in Figure 1a. The 0° pulse consisting of pulses 2 and 3 selects the C' magnetization for the t_1 evolution period. The magnetization is transferred from C' to C^α by the RFDR mixing period from pulse 4 to 6. After the t_2 evolution period, the C^α magnetization is transferred to C^β by the DQ dipolar interactions under SPC^{z}5. Pulses 1–4, 5–9, and 10–11 were respectively applied at the chemical shifts of 180, 57, and 39 ppm. Selective 0° pulses (2 and 3) and (7 and 8) at the center of the t_1 and t_2 evolution periods partially decouple homonuclear ^{13}CJ couplings (Straus et al., 1996). The pulse width of Gaussian 180° pulses 2 and 7 was about 120 μs, and that of the 90° pulse 6 was 500 μs. Pulses 1–3 and 4–7 were synchronously phase shifted by 90° steps for the phase-sensitive detection in the indirect time domains. The experimental data matrix $20(t_1)\times48(t_2)\times512(t_3)$ was zero-filled to $64\times128\times1024$. The number of transients for each FID was 16. Dwell time was 0.4 ms, 0.2 ms and 25 μs respectively for t_1, t_2, and t_3. Experimental time was 54 h. The S/N ratio of the cross peak for I6 was 2.8.

Pulse sequences for 3D N_i–C^α_i–C^β_i (Figure 1b), 2D N_i–$(C^\alpha C^\beta)_i$ (not shown), 2D $(C^\alpha C^\beta)_{i+1}$–$(C'C^\alpha)_i$ (Figure 1c) and 2D N_{i+1}–$(C'C^\alpha C^\beta)_i$ (Figure 1d) correlations have a ^{15}N-^{13}C mixing period with ramped-amplitude cross-polarization as shown in Figure 1. The magnetization was transferred from ^{15}N to ^{13}C under the ^{15}N RF field amplitude of about 13 kHz and the ^{13}C amplitude varying from 20 to 25 kHz, which satisfies the condition $\gamma B_{13C} \approx \gamma B_{15N} + \omega_R \approx$ 25 kHz. The difference in ^{13}C resonance frequency discriminates between carbonyl and aliphatic carbons during the cross polarization (Baldus et al., 1998). The ^{13}C–^{15}N J interactions during the ^{15}N evolution periods are decoupled by a π pulse at the center of the ^{15}N evolution period.

The mixing time for the 2D N_i–$(C^\alpha C^\beta)_i$ was 6 ms. RF fields were applied at the chemical shifts of 44 ppm

for ^{13}C and 88 ppm for ^{15}N. The time-domain matrix 512×512 was zero-filled to 1024×1024. The number of transients was 16 for each FID. The ^{15}N RF phase of ^{15}N–^{1}H cross polarization was alternated to select the coherence transfer pathway. The ^{15}N phase in ^{15}N–^{13}C cross polarization was cycled for the phase-sensitive detection and artifact suppression. Experimental time was 18 h. The S/N ratio of the cross peak for I6 was 4.5.

The pulse sequence for 3D N_i–C_i^{α}–C_i^{β} experiment is shown in Figure 1b. The mixing time for the ^{15}N–^{13}C dipolar couplings was 5 ms and that for the ^{13}C–^{13}C DQ dipolar couplings under SPC^{z}5 was 1.6 ms. The frequency of the ^{13}C RF field was 55 ppm and 40 ppm for the first and second mixing periods respectively, and that of ^{15}N was 120 ppm. The experimental data matrix $20(t_1)\times80(t_2)\times512(t_3)$ was zero-filled to $32\times128\times1024$. The number of transients for each FID was 8. Dwell time was 0.4 ms, 0.1 ms and 25 μs, respectively, for t_1, t_2, and t_3. The ^{15}N phase for the ^{15}N–^{1}H cross polarization and the ^{13}C phase for the ^{15}N–^{13}C cross polarization were cycled for the phase-sensitive detection. Experimental time was 43 h. The S/N ratio of the cross peak for I6 was 3.5.

The pulse sequence for 2D $(C^{\alpha}C^{\beta})_{i+1}$–$(C'C^{\alpha})_i$ correlation has a mixing period where cross polarization from $(C^{\alpha}C^{\beta})_{i+1}$ to $^{15}N_{i+1}$, cross polarization from $^{15}N_{i+1}$ to $^{13}C'_i$, and RFDR magnetization transfer from $^{13}C'_i$ to C_i^{α} are concatenated as shown in Figure 1c. The ^{13}C RF field was applied at the chemical shifts of 48, 178 and 120 ppm for the first and second cross polarization and the RFDR pulses, respectively, and the ^{15}N RF field was at 120 ppm. The lengths of the sequences for the first and second cross polarization and the RFDR pulses were 9.4 ms, 5.4 ms and 1.6 ms, respectively, for the spectrum in Figure 4a, and 6.0 ms, 5.4 ms and 1.6 ms for that in Figure 4b. The time-domain matrix $348(t_1)\times408(t_2)$ was zero-filled to 1024×1024. The number of transients was 96 for each FID. The ^{13}C RF phase for the first ^{15}C–^{15}N cross polarization was cycled for the phase-sensitive detection. The ^{13}C RF phases for the first ^{15}C–^{15}N cross polarization and the ^{15}N phases for the second ^{15}N–^{13}C cross polarization were alternated independently to select the transfer pathway of the magnetization. Experimental time was 61 h. The S/N ratio of the cross peak I6A7 was 4.0.

The pulse sequence for 2D N_{i+1}–$(C'C^{\alpha}C^{\beta})_i$ correlation is shown in Figure 1d. A ^{15}N 90° pulse is also employed to generate the initial ^{15}N magnetization (Rienstra et al., 2000). The mixing period consisted of the cross polarization from N_{i+1} to C'_i with a mixing time of 4.2 ms and the magnetization transfer from C'_i to C_i^{α} under an RFDR sequence with an mixing time of 1.92 ms. The frequency of the ^{13}C RF field was 180 ppm except for pulses in the RFDR mixing applied at 100 ppm. The time-domain matrix $280(t_1)\times512(t_2)$ was zero-filled to 1024×1024. The number of transients was 72 for each FID. The ^{15}N phases for the 90° pulse and the ^{15}N–^{1}H cross polarization were cycled synchronously for the phase-sensitive detection. The ^{15}N phase for the ^{15}N–^{13}C cross polarization was alternated to select the transfer pathway of the magnetization. Experimental time was 56 h. The S/N ratio of the cross peak for I6 C^{α} was 7.5.

All the experiments except 2D N_{i+1}–$(C'C^{\alpha}C^{\beta})_i$ correlation were performed at room temperature by using an Infinity 400 spectrometer (Varian Inc., U.S.A.) with broadband double and triple resonance probes for a 4-mm rotor under a static magnetic field of 9.4 T. The 2D N_{i+1}–$(C'C^{\alpha}C^{\beta})_i$ experiment was carried out with an Infinityplus 500 spectrometer at 10 °C under 11.75 T. Free induction decays were processed with Felix95 and 2000 (Accelrys Inc., U.S.A.). The time-domain data were Fourier-transformed with an exponential line-broadening factor of about 70 Hz. The ^{13}C chemical shift was referenced to the methyl signal of hexamethyl benzene resonating at 19.9 ppm which gives chemical shift relative to the methyl signal of 2,2-dimethylsilapentane-5-sulfonic acid (DSS) (Hayashi and Hayamizu, 1991; Wishart and Sykes, 1994). The ^{15}N chemical shift reference was computed from the ratios of resonance frequencies in the IUPAC recommendations (Markley et al., 1998).

Preparation of fully ^{13}C,^{15}N-labeled MP-X

Isotope-labeled MP-X was overexpressed in *E. coli* BL21(DE3) cells as a recombinant fusion protein with *Saccharomyces cerevisiae* ubiquitin under the T7 promoter. The details of the preparation are given in Reference (Kohno et al., 1998). The fusion protein had a decahistidine tag at its N-terminus. The *E. coli* cells were grown in M9 minimum media consisting of $^{15}NH_4Cl$ and [$^{13}C_6$]glucose. The protein was purified with a Ni^{2+}-NTA agarose affinity column. The ubiquitin-MP-X was cleaved specifically at the C-terminus of ubiquitin with yeast ubiquitin hydrolase, which was separately overexpressed in *E. coli* and isolated. The obtained MP-X was purified by reversed-

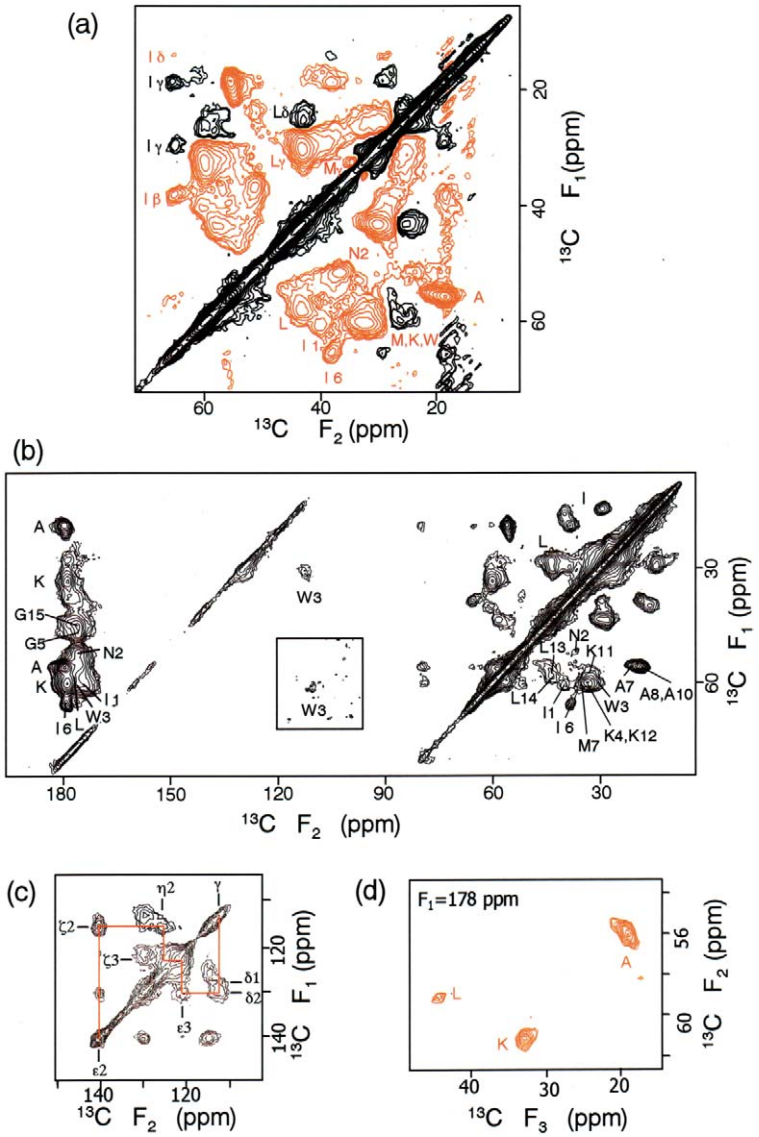

Figure 2. Multidimensional ^{13}C–^{13}C spectra for intra-residue correlations. (a) 2D band selective ^{13}C correlation spectrum for the aliphatic region of fully ^{13}C,^{15}N-labeled MP-X. The pulse sequence for this spectrum has a ^{13}C DQ dipolar mixing period under an SPC^{z}5 pulse sequence. Red lines show negative contour levels. (b) 2D broadband ^{13}C correlation spectrum obtained with a pulse sequence having an RFDR mixing period at a length of 2.4 ms. Contour levels for the C^{α}–C^{γ} cross peak of Trp in the square are half of the levels in the other area. (c) Tryptophan indole ^{13}C region of the 2D broadband ^{13}C correlation spectrum obtained with the same pulse sequence that the spectrum (b) was acquired with. The red lines show the sequential connectivity along the covalent bonds. (d) 2D cross section of the 3D C'_i–C_i^{α}–C_i^{β} correlation spectrum sliced at $F_1 = 178$ ppm. The 3D pulse sequence for this spectrum is shown in Figure 1a.

phase HPLC. About 6 mg of MP-X obtained from 10 l medium was dissolved in 2.0 ml of methanol. The MP-X was precipitated at 10 °C by gradually evaporating the solvent over two days. The precipitate was used for solid-state NMR experiments.

Structural calculations

The TINKER molecular modeling software package (Ponder and Richards, 1987) was used for the structure generation from the backbone dihedral angles, RMSD calculation, superposition of structures and energy minimization. The backbone RMSD between two structures was calculated for C^{α}, C' and N in residues

2–14. The energy of MP-X structure predicted from the chemical shifts in the solid state was minimized by optimizing conformations of the backbone of the residues at the N- and C-termini and the side chains of all the residues with AMBER-94/96 force fields (Cornell et al., 1995). We have generated two MP-X structures by optimizing the energy starting from different side chain orientations to assess the effects of side chain conformation on chemical shifts. These structures were used for C^{β}, C^{α}, C', and N chemical-shift prediction by SHIFTS (Xu and Case, 2001, 2002) and for C^{β} and C^{α} prediction by TANSO (Iwadate et al., 1999). The chemical shift RMSD between two structures was computed for resonances in residues 2–14. In the computation of RMSD for SHIFTS, only ^{15}N chemical shift differences were divided by two. This weighting factor for ^{15}N approximately equalizes the contributions of C^{α}, C^{β}, C' and N chemical shifts to RMSD, because RMSD between experimental and predicted chemical shifts for ^{15}N (ca. 2.7 ppm) is about twice as large as that for ^{13}C (ca. 1.3 ppm) (Xu and Case, 2002). The graphics of the MP-X structure was prepared with software RasMol (Sayle and Milner-White, 1995). The membrane-bound and G-protein-bound structures for the comparison were selected from the NMR derived structures, which were similar to the average structures.

Results

Intra-residue spin connectivities for the assignments to amino acids

The 2D ^{13}C correlation spectrum for the aliphatic region shown in Figure 2a was obtained with the pulse sequence having a band selective ^{13}C–^{13}C DQ dipolar mixing period. The selective $^{13}C^{\alpha}$–$^{13}C^{\beta}$ DQ dipolar recoupling provides the transferred magnetization stronger than broadband recoupling because the dipolar couplings with $^{13}C'$ spins were decoupled during the selective mixing period (Hohwy et al., 2002; Matsuki et al., 2003). Figure 2b shows 2D broadband ^{13}C–^{13}C correlation spectrum obtained with zero-quantum dipolar couplings under an RFDR sequence. The recoupling efficiency of RFDR is low for the cross peaks near the diagonal line, because the chemical shift differences are much smaller than the spinning rate (Bennett et al., 1998). However, the DQ recoupling method gives DQ dipolar interaction in the selected region almost independently of the chemical shift difference. This is exemplified by the cross peak C^{β}–C^{γ} of Met near the diagonal line. This cross peak is clearly seen in Figure 2a obtained with the DQ dipolar recouping but not in Figure 2b obtained with the RFDR sequence. The RFDR spectrum gives strong cross peaks between $C^{\alpha}C^{\beta}$ and C' for which chemical shift differences are comparable to the sample spinning frequency. Thus the RFDR and the selective DQ recoupling methods give complementary information about dipolar coupling connectivities.

We can find all intra-residue cross peaks between C^{α} and C^{β} in Figures 2a and b, though the Met, Lys and Trp signals overlap. Cross peaks of the same amino acid type are not well resolved except for Ile. We can trace the connectivities for Ile at 65 ppm in Figure 2a. The cross peaks of C^{α} correlating with C^{β}, C^{γ} and C^{δ} exhibit negative, positive and negative intensities, respectively. This intensity pattern indicates that the magnetization is transferred through the ^{13}C spins along the covalent bonds in the side chain. Mutual cancellation due to the $\pm$ modulation was not so conspicuous for Figure 2a. This is partly due to a short mixing time optimized for the transfer between ^{13}C spins separated by one covalent bond. The RFDR spectrum has cross peaks between C' and C^{α} in addition to cross peaks in the aliphatic region. The C^{α} chemical shifts of Gly, Asn and Ile6 residues are well separated from others, which enables unambiguous assignments of C' of these residues (Figure 2b). At the mixing time of 2.4 ms, cross peaks between C^{β} and C' were also observed. Those cross peaks for Ala and Lys can be identified by the correlations with C^{β} resonances. We have assigned Trp C^{α} and C^{β} cross peaks from their correlation with C^{γ} in the indole ring region. An RFDR spectrum at a shorter mixing time of 0.8 ms gave almost the same spectral shape for the C^{α}–C' region (data not shown). This allows the negligence of inter-residue correlations in this region at a mixing time of 2.4 ms shown in Figure 2b.

As shown in Figure 2c, the ^{13}C signals for the indole ring were assigned sequentially in the 2D spectrum obtained with the RFDR sequence. Figure 2d shows a 2D cross section taken from the 3D C'_i–C^{α}_i–C^{β}_i correlation spectrum. We can assign the C' resonance of Leu from the spectrum. This assignment is not obvious only from the 2D RFDR spectrum because Leu C^{β} has the chemical shift close to that of Gly C^{α}. Cross peaks in this section have negative intensities because ^{13}C DQ dipolar interactions were used in the second mixing period of the 3D sequence shown in Figure 1a.

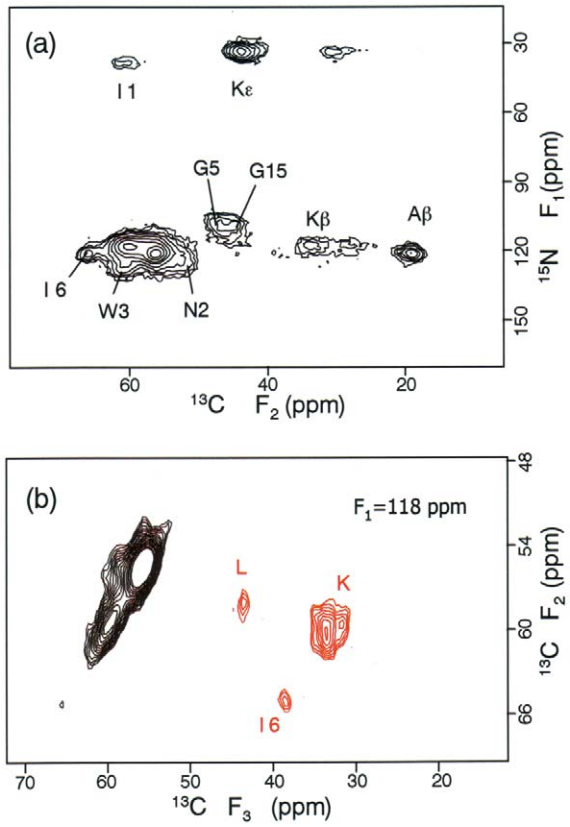

Figure 3. Multidimensional intra-residue correlation spectra for ^{13}C and ^{15}N. 2D N_i–$(C^\alpha C^\beta)_i$ spectrum of MP-X (a), and 2D C^α_i–C^β_i cross section of the 3D N_i–C^α_i–C^β_i spectrum sliced at F_3 = 118 ppm (b). Red lines show negative contour levels. Cross peaks between C^α_i and C^β_i show the magnetization transfer by ^{13}C DQ dipolar interactions recoupled band-selectively.

We have decoupled homonuclear J couplings for $^{13}C'$ and $^{13}C^\alpha$, respectively, during the t_1 and t_2 periods in the 3D C'_i–C^α_i–C^β_i experiment (Straus et al., 1996). However, the resolution enhancement of the spectrum was not conspicuous at the expense of signal intensities, because the linewidths were primarily due to the inhomogeneous broadening by the chemical shifts. Thus we did not adopt the decoupling pulses in the other pulse sequences.

Figure 3 shows a 2D N_i–$(C^\alpha C^\beta)_i$ spectrum and a 2D cross section of a 3D N_i–C^α_i–C^β_i spectrum obtained with pulse sequences having a mixing period under $^{15}N_i - ^{13}C^\alpha_i$ dipolar couplings as illustrated in Figure 1b. In Figure 3a, we can specify the chemical shifts of backbone ^{15}N nuclei from the cross peaks for isolated ^{13}C resonances. Nitrogen chemical shifts were also determined from the 3D N_i–C^α_i–C^β_i spectrum as shown in Figure 3b. The cross peaks in the 3D N_i–C^α_i–C^β_i spectrum have negative intensities because of the ^{13}C DQ dipolar recoupling employed in the second mixing period. The ^{13}C–^{15}N spin decoupling by the 180° pulse during the evolution period did not enhance the spectral resolution clearly. Since it did not deteriorate the signal intensities, it was used in other sequences.

Inter-residue spin connectivities for sequence specific assignments

The pulse sequence for a 2D $(C^\alpha C^\beta)_{i+1}$–$(C'C^\alpha)_i$ correlation experiment is shown in Figure 1c. The t_1 and t_2 evolution periods for ^{13}C are connected by a mixing period during which the magnetization is transferred from C^α and C^β in the $(i+1)$th residue to C' and C^α in the ith residue. The mixing period consists of three component pulse sequences for the transfer from $(C^\alpha C^\beta)_{i+1}$ to N_{i+1}, from N_{i+1} to C'_i, and from C'_i to $(C^\alpha C^\beta)_i$. This is a triple resonance experiment though the correlations are observed only between ^{13}C spins.

Figure 4a shows the correlation spectrum between $(C^\alpha C^\beta)_{i+1}$ and $(C'C^\alpha)_i$. The 2D spectrum is not symmetric with respect to the diagonal line because the magnetization is transferred unidirectionally between neighboring residues during the mixing period. Carbonyl carbons are resolved along the F_1 axis by the C^α chemical shift of the following amino acid residue. Thus, carbonyl signals in the residue prior to G N, and I6 are easily assigned, since their C^α signals have isolated chemical shifts. The C^β resonances in the F_1 dimension are resolved along the F_2 axis by the C^α chemical shift of the preceding residue. This is shown for alanine methyl resonances for I6A7, A7A8, and M9A10 in Figure 4a. The cross peak for I6A7 is smaller than the other two in the intensity, probably because of the relaxation during the mixing period. Since the total mixing time of this sequence, 16.4 ms, is the longest of all the mixing times in this study, the signal intensity is sensitive to the relaxation. The signal intensities of this spectrum are not so strong as those obtained by other methods for intra-residue correlations because the mixing period of this sequence contains the three dipolar mixing schemes each of which has a transfer efficiency less than about 0.5.

We have assigned C^α resonances sequentially from the C^α_{i+1}–C^α_i region of the 2D $(C^\alpha C^\beta)_{i+1}$–$(C'C^\alpha)_i$ correlation spectrum as shown in Figure 4b. The C^α chemical shifts 1–7, 14 and 15 can be determined from the isolated cross peaks. Although other cross

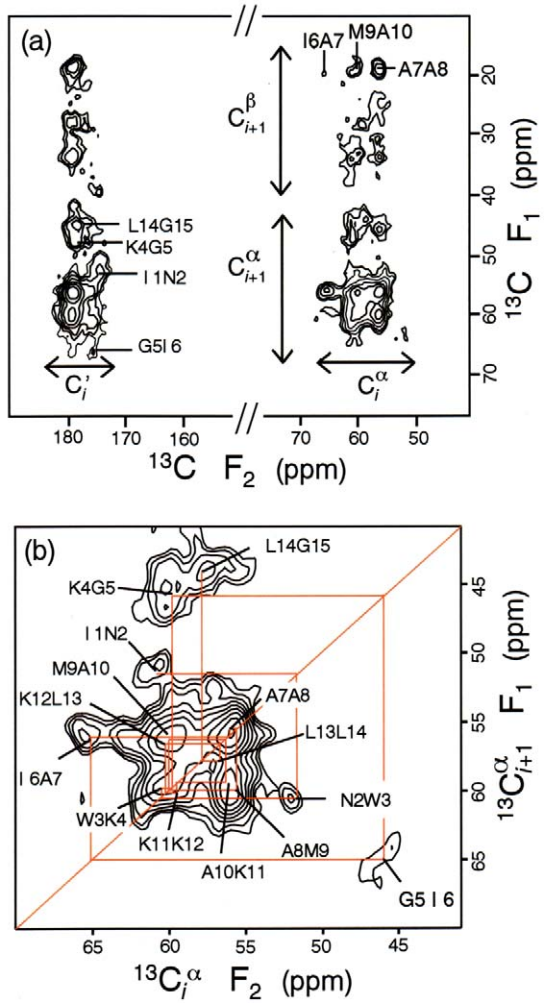

Figure 4. (a) 2D $(C^{\alpha}C^{\beta})_{i+1}$–$(C'C^{\alpha})_i$ correlation spectrum of MP-X. (b) C^{α}_{i+1} vs C^{α}_i region of 2D $(C^{\alpha}C^{\beta})_{i+1}$–$(C'C^{\alpha})_i$ spectrum. Sequential assignment of C^{α} is indicated by red lines. The length of the first mixing sequence between $(C^{\alpha}C^{\beta})_{i+1}$ and N_{i+1} for (a), 9.4 ms, is longer than that for (b), 6.0 ms, to enhance to the magnetization transfer from C^{β}_{i+1} rather than from C^{α}_{i+1}.

peaks are not separated clearly, we can determine the chemical shifts of those cross peaks from other correlation spectra. The red line shows the sequential signal assignments. The details will be shown in the following section. The red line starts at the signal I1N2 and bends at the signals K4G5, G5I6 and I6A7 off the peak maxima by about 0.4 ppm. These inconsistencies between peak top chemical shifts in the F_1 and F_2 dimensions are smaller than the linewidths given in Table 1. Peak positions of broad signals with small intensities such as G5I6 would deviate owing to noises and broad baselines at the tails of large peaks. Another possible factor is the chemical shift distribution that correlates with conformational and motional heterogeneity. The C^{α}_i lineshape of the C^{α}_{i+1}–C^{α}_i cross peak in the F_2 dimension and that of the C^{α}_i–C^{α}_{i-1} peak in the F_1 dimension were obtained by filtering the initial proton magnetization through different dipolar interactions and relaxation processes during the preparation and mixing periods. This difference in the magnetic interactions may unevenly modify the signal intensities from conformers with slightly different chemical shifts. Similar nonuniformity in the spin state prepared by dipolar couplings makes 2D solid-state chemical-shift correlation spectra asymmetric with respect to the diagonal line (Caldarelli and Emsley, 1998).

The two-dimensional N_{i+1}–$(C'C^{\alpha}C^{\beta})_i$ spectrum shown in Figure 5 was obtained with the pulse sequence given in Figure 1d. The magnetization is transferred during the mixing period from ^{15}N in the $(i+1)$th residue to $^{13}C^{\alpha}$ and $^{13}C^{\beta}$ in the ith residue through the $^{13}C'$ spin. Thus two mixing schemes are concatenated in the mixing period. The cross peaks for C^{α} are stronger than those for C^{β} in signal intensity because of the shorter distances for C^{α}–C'. This experiment is useful for resolving the ^{15}N resonances by the chemical shifts of $^{13}C^{\alpha}$ and $^{13}C^{\beta}$ in the preceding residues. In the C^{α} region, we can assign ^{15}N resonances of the residues following G, N and I6 from their C^{α} chemical shifts. Similarly in the C^{β} region, ^{15}N resonances are assigned from the C^{β} chemical shifts identified previously. The ^{13}C and ^{15}N chemical shifts for the cross peaks are indicated in Figure 5. Note that this spectrum contains intra-residue cross peaks for ^{15}N in side chains, C^{α}–N^{δ} and C^{β}–N^{δ} in Asn2. The carbonyl region of this spectrum is not shown, because the region is not so informative as the C^{α} and C^{β} region owing to the smaller carbonyl chemical shift dispersion.

Complete signal assignments from the connectivities

We have presented all the information for the assignments of C^{α}, C^{β}, C' and N signals. We start the assignments from the C^{α} signals. The N_{H3}–C^{α} cross peak in the intra-residue N–C correlation spectrum (Figure 3a) and the C^{α}–C^{γ} cross peak in the RFDR spectrum (Figure 2b) provide the C^{α} chemical shifts of I1 and W3, respectively. Glycine C^{α} spins generally resonate at about 45 ppm. These chemical shifts allow the sequential assignments in the C^{α}_{i+1}–C^{α}_i correlation spectrum (Figure 4b), which provides the C^{α} chemical

Table 1. ^{15}N, $^{13}C'$, $^{13}C^{\alpha}$ and $^{13}C^{\beta}$ chemical shifts and apparent linewidths of mastoparan-X in ppm

	N	C′	C^{α}	C^{β}
Ile1	38.0 (5.0, *n*)	174.8 (4.5, *a*)	60.6 (3.3, *n*)	40.0 (2.3, *s*)
Asn2	128.0 (9.0, *n*)	175.6 (4.3, *r*)	51.7 (2.4, *a*)	37.3 (3.3, *r*)
Trp3	127.0 (5.0, *p*)	176.5 (2.6, *r*)	60.8 (2.5, *r*)	31.5 (3.5, *r*)
Lys4	117.3 (5.0, *n*)	178.5 (3.0, *a*)	60.2 (2.2, *a*)	32.5 (3.5, *r*)
Gly5	108.4 (7.0, *n*)	175.8 (2.8, *a*)	46.0 (2.7, *a*)	
Ile6	122.0 (4.5, *n*)	178.9 (2.0, *r*)	65.3 (2.0, *a*)	38.5 (2.0, *s*)
Ala7	121.5 (4.0, *p*)	179.4 (2.4, *r*)	56.0 (1.5, *a*)	19.3 (2.6, *a*)
Ala8	121.5 (4.0, *n*)	179.7 (2.4, *r*)	55.8 (1.5, *r*)	18.2 (2.6, *a*)
Met9	117.2 (5.0, *n*)	179.0 (2.6, *r*)	60.4 (2.4, *a*)	32.4 (2.7, *s*)
Ala10	121.5 (4.0, *n*)	179.7 (2.4, *r*)	56.0 (1.5, *r*)	18.2 (2.6, *a*)
Lys11	118.9 (5.0, *n*)	179.0 (3.0, *r*)	59.6 (2.7, *r*)	33.0 (3.5, *r*)
Lys12	118.5 (5.0, *n*)	179.0 (3.0, *r*)	60.7 (2.7, *r*)	32.0 (3.5, *r*)
Leu13	118.5 (5.5, *m*)	178.5 (2.7, *d*)	57.5 (3.4, *r*)	43.5 (3.0, *r*)
Leu14	118.5 (5.5 *m*)	178.5 (2.7, *a*)	58.0 (3.4, *a*)	43.5 (3.0, *r*)
Gly15	109.5 (7.0, *n*)	175.8 (4.5, *r*)	44.5 (2.7, *a*)	

Apparent linewidths and spectra primarily used for the assignments are given in the parentheses. The spectra are represented by symbols as 2D RFDR (*r*), 2D SPC^{z}5 C^{α}_{i}–C^{β}_{i} (*s*), 3D C'_{i}–C^{α}_{i}–C^{β}_{i} (*d*), 2D N_i–$(C^{\alpha}C^{\beta})_i$ (*n*), 3D N_i–C^{α}_{i}–C^{β}_{i} (*m*), 2D $(C^{\alpha}C^{\beta})_{i+1}$– $(C'C^{\alpha})_i$ (*a*), and 2D N_{i+1}–$(C'C^{\alpha}C^{\beta})_i$ (*p*) correlations.

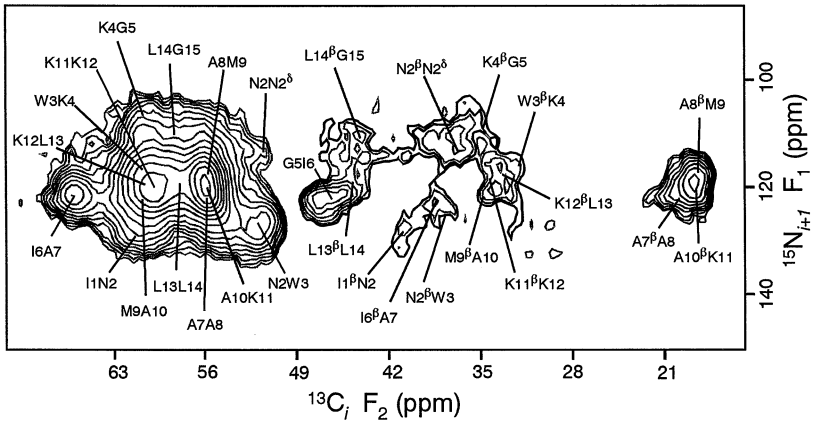

Figure 5. Aliphatic region of 2D N_{i+1}–$(C'C^{\alpha}C^{\beta})_i$ spectrum of MP-X. The pulse sequence for this spectrum is shown in Figure 1d.

shifts of N2, K4, G5, I6, A7, L14 and G15. The RFDR spectrum shows that A7, A8 and A10 have the C^{β} resonances at about 19 ppm. Since the C^{α} chemical shifts of I6 and A7 have been determined, we can assign the isolated I6A7, A7A8 and M9A10 signals in the 2D $(C^{\alpha}C^{\beta})_{i+1}$–$(C'C^{\alpha})_i$ correlation spectrum (Figure 4a). These three signals provide the M9 C^{α} and three alanine C^{β} chemical shifts. We determined the C^{α} chemical shifts of A8 and A10 from the C^{α}–C^{β} cross peak at their respective C^{β} shifts in Figure 2b. The RFDR spectrum have signal intensities for Leu residues at about 58 ppm. Having determined the L14 C^{α} shift from the C^{α}_{i+1}–C^{α}_{i} correlation spectrum, we selected the most probable chemical shifts for L13 and L14 C^{α}–C^{β} cross peaks so as to reproduce the RFDR spectral shape on the assumption that each of L13 and L14 C^{α} gives a single peak. The difference 0.5 ppm between two Leu C^{α} shifts depends on their chemical shift distributions, and is smaller than the precisions in shift determined by the apparent linewidths in Table 1.

The C^{β} resonances of A7, A8, A10, L13 are L14 have been assigned above. The C^{β} resonances of I1,

N2, W3, I6 and M7 are assigned from isolated cross peaks in Figures 2a and 2b. The K4 C^{β} chemical shift was obtained from the C^{α}–C^{β} peak at its C^{α} resonance frequency. Thus, we have determined all the C^{α} and C^{β} shifts except for K11 and K12. The C^{α}–C^{β} correlation spectra in Figure 2a and b approximately give Lys C^{α} chemical shift of 60 ppm and the C^{β} shift of 32 ppm. To determine the shifts more precisely, we simulated the C^{α}–C^{β} cross peaks near the K resonances and the C^{α}_{i+1}–C^{α}_{i} spectrum for the C^{α} shifts of K11 and K12 within 60 ± 1 ppm and the C^{β} shifts within 32 ± 1 ppm. We have selected the chemical shifts that reproduced the experimental spectral shapes. The precisions of these chemical shifts are restricted by the signal degeneracies. The sequential connectivities for all the C^{α} chemical shifts are shown by the red lines in Figure 4b.

Carbonyl chemical shifts of I1, K4, G5 and L14 were determined from the C^{α}_{i+1}–C'_{i} correlations in Figure 4a. The N2, I6 and G15 carbonyl shifts were obtained from the C′–C^{α} cross peaks in the RFDR spectrum. The C′ shifts of W3, A7, A8, M9, A10, K11 and K12 were determined from the C′–C^{β} signal peaks at the respective C^{β} shifts in the RFDR spectrum. The 3D C′–C^{α}–C^{β} spectrum gives the shift of the L13 carbonyl signal overlapping with the L14 signal. These assignments are compatible with the signal intensities in the intra-residue C′tC^{α} spectrum (Figure 2b).

The ^{15}N resonances were assigned from the cross peaks in Figures 3 and 5 at the C^{α} and C^{β} chemical shifts previously determined. The intra-residue N–C^{α} cross peaks in Figure 3 provide the ^{15}N chemical shifts of I1, N2, G5, I6 and G15. The L13 and L14 shifts were obtained from the 3D spectrum (Figure 3b). The N–C^{β} cross peaks for K4, A8, M9, A10, K11 and K12 in Figure 3 provide the ^{15}N chemical shifts. The inter-residue N_{i+1}–C^{α}_{i} cross peaks in Figure 5 give the chemical shifts of W3 and A7. Since we have already determined all the C^{β} and N chemical shifts, we can confirm those shifts by the N_{i+1}–C^{β}_{i} cross peaks in Figure 5. The ^{15}N chemical shifts of K4, M9, K11 and K12 were finally modified within 1 ppm according to the N_{i+1}–C^{β}_{i} cross peaks.

Accuracies in ^{13}C′ and ^{15}N chemical shifts are affected by the C^{β} and C^{α} chemical shift dispersions as well as by their own shift dispersions, because ^{13}C′ and ^{15}N resonances are resolved by the C^{β} and C^{α} chemical shifts in the spectra. The W, K and M residues had similar C^{α} and C^{β} chemical shifts. The C′ and N resonances of three A and two l residues were difficult to distinguish sequence-specifically only by their C^{α} and C^{β} chemical shifts as shown in the intra-residue correlation spectra. However, the C′ and N signal degeneracies were partly resolved by the C^{α} chemical shifts of the following and preceding residues, respectively. The signal assignments are summarized in Table 1 showing the chemical shifts, apparent linewidths and spectra primarily used.

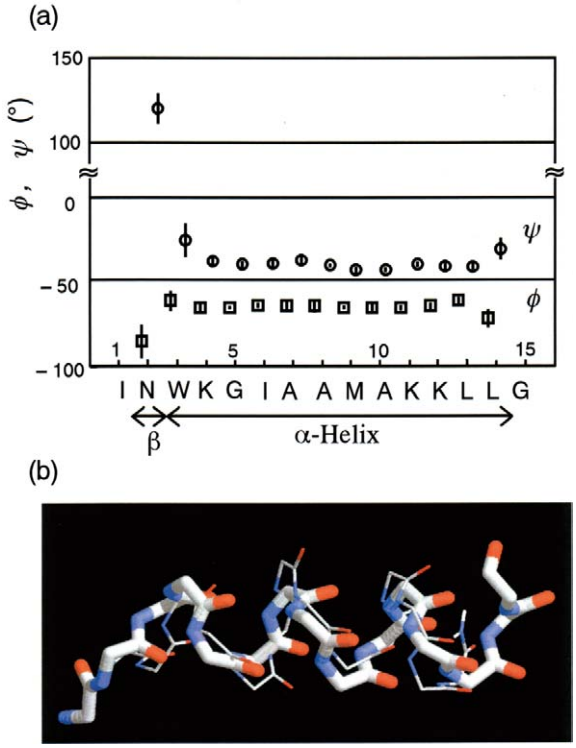

Figure 6. (a) Backbone dihedral angles, ϕ and ψ, of MP-X in the solid state predicted with TALOS as a function of residue number. Error bars give standard deviations of the angles selected from the database by TALOS, and do not directly indicate the accuracies in the angles. (b) Backbone structures of the solid-state glycinated MP-X and G-protein-bound MP-X molecules, respectively, represented by thick and thin sticks. The two structures are superposed by minimizing the backbone RMSD.

Discussion

Secondary structure from the chemical shifts

Conformation dependent chemical shifts of proteins have been used for the secondary structure analysis in solution NMR (Wishart and Sykes, 1994). Similar secondary chemical shifts were verified also for peptides and proteins in solid states (Saito and Ando, 1989; Luca et al., 2001). We have predicted the

main chain ϕ and ψ angles by the analysis of $^{13}C^{\alpha}$, $^{13}C^{\beta}$, $^{13}C'$and ^{15}N chemical shifts with the program TALOS (Cornilescu et al., 1999). The prediction by TALOS is based on the similarity in chemical shifts and amino acid sequences for selected proteins stored in the BioMagResoBank (BMRB) database. Predicted ϕ and ψ angles from the chemical shifts in Table 1 are shown in Figure 6. The chemical shifts indicate that the main chain of MP-X in the solid state has extended conformation at residue 2 and forms α-helix in residues 3–14. The backbone structure generated from the ϕ and ψ angles is also presented. The calculated structure does not have steric hindrance although only the local structures were predicted from the chemical shifts.

A circular dichroism study has shown that MP-X assumes a helical structure in a methanol solution but random coil in an aqueous solution (Higashijima et al., 1983). Solution NMR studies provide more detailed MP-X structures. Bicelle associated MP-X was analyzed with NOESY and ^{1}H chemical shifts (Whiles et al., 2001). Membrane-bound and G-protein-bound forms were studied with transferred NOE. All these NMR studies indicate that the backbone from residue 3 to 14 forms helical structure but that at residue 2 does not, which agrees with our study on the structure in the solid state. Since MP-X forms such α helical structure in more or less hydrophobic environments, MP-X in a methanol solution would also take a structure similar to that in the solid state. Close inspection of the solution NMR structures, however, reveals that the membrane-bound MP-X has an α helix but the G-protein-bound MP-X has a backbone similar to π helix in the hydrogen bonding pattern, pitch and diameter. Such characteristics are seen in Figure 6b where the G-protein-bound structure is superposed with the solid-state structure that have a typical α helix. Thus the backbone RMSD between the solid-state and membrane-bound structures, 0.8 Å, is smaller than that between the solid-state and G-protein-bound structures, 2.2 Å.

Accuracy of the predicted backbone structure

We have evaluated the accuracy of the solid-state structure predicted by TALOS. The programs SHIFTS and TANSO were used for predicting chemical shifts from the atomic coordinates of the solid-state, membrane-bound and G-protein-bound forms of MP-X. The program TANSO predicts only the $^{13}C^{\alpha}$ and $^{13}C^{\beta}$ chemical shifts with the database of experimental

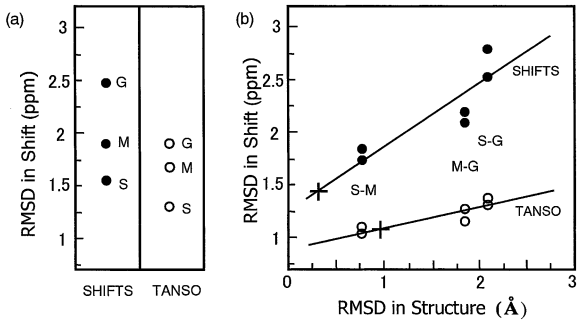

Figure 7. (a) RMSD between the experimental and predicted chemical shifts, and (b) correlation between RMSD for the backbone structures and that for chemical shifts of MP-X. (a) Circles labeled with G, M and S designate the RMSD calculated from the chemical shifts predicted for the G-protein-bound, membrane-bound and solid-state MP-X structures, respectively. Dark and open circles were obtained for the chemical shifts predicted with the programs SHIFTS and TANSO, respectively. (b) RMSDs were calculated for the solid-state (S), membrane-bound (M) and G-protein-bound MP-X (G). Lines were fitted to circles showing the correlations for structures and chemical shifts predicted with the two programs. Crosses are plotted on the lines at the chemical shift RMSD between the experimental and predicted shifts for MP-X in the solid state. The uncertainties in experimental chemical shift were estimated to be $\pm$0.9, $\pm$0.6, $\pm$1.0 and $\pm$1.7 ppm for C$'$, C^{α}, C^{β} and N from the linewidths (see the the text for details). These contributions were subtracted from the RMSD between the experimental and calculated chemical shifts only for (b).

protein chemical shifts in BMRB (Iwadate et al., 1999). The program SHIFTS predicts the $^{13}C^{\alpha}$, $^{13}C^{\beta}$, $^{13}C'$ and ^{15}N chemical shifts with the database of the shifts calculated quantum chemically for short model peptides. The ^{15}N chemical shifts can be used for predicting the backbone structure because the secondary structure is a dominant factor in the shift. Recent quantum chemical study (Xu and Case, 2002) indicated that contribution of hydrogen bonding to ^{15}N chemical shift (up to 8 ppm) is smaller than that of backbone conformation (up to 13 ppm). Effects of hydrogen bonding are also explicitly included in the predictions.

The RMSD between the experimental and predicted chemical shifts are shown in Figure 7a for which the predicted shifts were obtained with SHIFTS and TANSO. The experimental chemical shifts in Table 1 are most similar to chemical shifts predicted for the solid-state structure, and are most different from those for the G-protein-bound MP-X as shown in Figure 7a. This similarity in chemical shifts indicates that the structure predicted by TALOS is the best model for the solid-state MP-X among the three structures, since there is a positive correlation between

RMSD for the chemical shifts and that for atomic coordinates as will be demonstrated for Figure 7b.

The differences between the RMSDs for the solid-state and membrane-bound structures in Figure 7a are significant from the precisions in the prediction. According to the χ^2 test, we can distinguish the RMSDs for the two structures with a probability of about 90% on the assumption that prediction errors in RMSD are 1.5 ppm and 1.2 ppm for SHIFTS and TANSO, respectively. These RMSD values due to prediction errors were estimated from the RMSD between the experimental and predicted shifts for the solid-state structure. Since the estimated RMSD may include contributions of factors other than the prediction errors, true RMSD only due to the errors would be smaller than the RMSD values used above. In this case, we can distinguish the two RMSDs with a probability higher than 90%.

As stated above, SHIFTS and TANSO differ in database and the spin whose chemical shift is predicted, as well as in the algorithm for the prediction. Therefore, the RMSD values calculated with them are different as shown in Figure 7. Despite these differences, the two methods derived the same conclusion that the structure predicted by TALOS is the best model structure for reproducing the experimental chemical shifts. This suggests that the conclusion is valid even under the limitations of the methods.

We have estimated the accuracy of the structure predicted by TALOS from the correlation between RMSD for chemical shifts and that for three-dimensional structures. This correlation is shown in Figure 7b. The horizontal axis gives the RMSD in atomic coordinates of structures. This axis indicates that the RMSD between the solid-state (S) and membrane-bound (M) structures is smallest, and the RMSD between G-protein-bound (G) and S structures is slightly larger than that between M and G structures. The vertical axis gives the RMSD in chemical shift calculated with the programs SHIFTS and TANSO for the three pairs of the helical structures. There is a positive correlation between the RMSD in shift and that in structure. The positive correlation such as this provides a basis for the chemical shift perturbation method for monitoring structural changes (Foster et al., 1998). The RMSD in structure obtained from the correlation at the RMSD in shift between the calculated and experimental shifts would indicate the accuracy of the structure predicted for the solid state. The RMSD between the calculated and experimental shifts is shown by crosses in Figure 7b. Those crosses give the accuracies of about 0.3 and 1.0 Å for backbone RMSD following the correlation obtained with SHIFTS and TANSO, respectively. Thus, the structure predicted by TALOS would be accurate with a backbone RMSD of about 1 Å.

Effects of side chain dihedral angles on chemical shifts are considered to be relatively small. Chemical shifts were calculated for the same main chain structure with two side chain structures different in χ_1 angles by about 40^o on average. These chemical shifts give two RMSDs in shift at each RMSD in structure as shown in Figure 7b. The difference between the two provides a measure for the effect of side chain structure. The RMSD between calculated chemical shifts at the RMSD in structure of zero shows the contributions of differences in structures of side chains, and N- and C-terminal residues. These contributions together with errors in chemical shift prediction would limit the resolution of the backbone structure derived from the chemical shifts.

The signal linewidth due to chemical shift dispersion would serve as a measure of the precision in adopting the chemical shift at the peak-maximum. The contributions of the dispersion were estimated by subtracting contributions of *J* couplings (Cavanagh et al., 1996) and line broadening by the window function from the apparent linewidths in Table 1. The averaged linewidths (FWHM) for the dispersions are about 1.7, 1.1, 1.9 and 3.2 ppm for C', C^{α}, C^{β} and N resonances, respectively. Since the signals are not completely resolved, signal overlaps of different spins in addition to conformational multiplicity may contribute to the linewidths.

The ensemble of the solid-state MP-X molecules are considered to have a minor structural distribution in backbone besides that in sidechains, for the following reasons: (i) The estimated linewidths mainly due to structural distribution, about 1 to 2 ppm for ^{13}C and about 3 ppm for ^{15}N, accord with those for well-ordered noncrystalline peptides but are larger than those for amino acids, proteins, and peptides in crystals (Balbach et al., 2000a,b; Pauli et al., 2000). (ii) The estimated linewidths are smaller than the chemical shift variations due to the backbone conformation, about 4 ppm for ^{13}C and about 8 ppm for ^{15}N (Xu and Case, 2002). (iii) The linewidths are comparable to the RMSD in shift that corresponds to the RMSD in structure of about 1–2 Å (Figure 7b).

Biological significance of the predicted structure of MP-X

Mastoparan-X was reported to bind lipid membrane and to translocate ions, lipids and itself across the membrane (Matsuzaki et al., 1996). It was inferred that the translocation takes place as a pore composed of oligomeric peptides. This was discussed in connection with the membrane-bound structure of MP-X determined by transferred NOE (Wakamatsu et al., 1992). We can address this point referring to the structure predicted by the solid-state NMR as well. Judging from the signal linewidths, MP-X in the solid state takes a well-ordered structure even though the sample is not well-defined crystals. Therefore, it must have formed an ordered oligomeric structure when it was precipitated from the methanol solution. Owing to the amphiphilic α-helix of the peptide, a pore-like structure formation is plausible. The backbone structure of the peptide is similar to that found for the membrane-bound peptide as described above. This result strongly suggests that the membrane-bound conformation is stable not only on the surface of the membrane but also in the pore formed in the hydrophobic region of the membrane. This would make the pore formation energetically preferable, because there is no need of conformational rearrangement. Furthermore, the extended structure of Ile1 and Asn2 would help the pore fit the membrane thickness (Matsuzaki et al., 1996). Thus, the α-helix with an extended N-terminus would have a biological significance. Structure determination of MP-X strongly binding to lipid bilayers by solid-state NMR with distance measurements is under way by our group. Such study would elucidate the difference between the solid-state and membrane-bound structures.

Conclusions

Carbon-13 and nitrogen-15 signals for the backbone and C^β atoms of uniformly labeled 15-residue peptide, glycinated MP-X, were assigned completely with inter- and intra-residue dipolar spin connectivities obtained by multidimensional MAS NMR experiments. The peptide had the ^{13}C and ^{15}N linewidths larger than those of peptides in highly-ordered crystal states. The C^α and C^β chemical shift dispersion was useful for resolving signals as demonstrated by the 2D N_{i+1}–$(C'C^\alpha C^\beta)_i$ correlation and 2D $(C^\alpha C^\beta)_{i+1}$–$(C'C^\alpha)_i$ correlation spectra. The applicability of this method to larger peptides and proteins would depend on the following factors affecting the spectral resolution and sensitivity: Sample preparations that improve the structural homogeneity such as crystallization reduce the linewidths due to the distribution of chemical shifts, and enhance both the resolution and sensitivity (Pauli et al., 2000; Detken et al., 2001). The amino acid composition and the secondary structure content influence the chemical shift dispersion of peptides. Most of the resonances of MP-X clustered around the chemical shifts for α-helix. Experiments under higher static fields and faster MAS would reduce the linewidths in ppm due to J and ^{13}C–^{13}C dipolar couplings, which is desirable for the signal assignments of fully ^{13}C,^{15}N-labeled peptides. For the present experiments at the static field of 9.4 T, J couplings would broaden the C^α resonance lines by about 1 ppm. Extensive use of 3D NMR experiments would improve the resolution at the expense of the sensitivity. Nuclear magnetic relaxation by thermal motions and dipolar couplings with protons during the mixing periods also limits the signal sensitivity, in particular, of experiments having longer mixing times such as the $(C^\alpha C^\beta)_{i+1}$–$(C'C^\alpha)_i$ correlation experiment (Hohwy et al., 1999). Thus, sample temperature and ^1H decoupling fields are also important factors.

Chemical shifts obtained by the signal assignments are easily accessible in comparison with internuclear distances. We have predicted the backbone structure of MP-X from the ^{13}C and ^{15}N chemical shifts with the program TALOS. Recent developments of the theoretical study of chemical shift and an increase in the number of NMR protein structures in databases improve the reliability of proteins structure analysis by the chemical shifts. We have estimated the accuracy of the predicted structure to be about 1 Å in the backbone RMSD, on the basis of both the empirical and quantum mechanical analyses of the chemical shifts. The linewidths originating from chemical shift dispersion suggest that MP-X molecules in the solid-state have a minor backbone conformational distribution. The structure predicted for the solid state is close to the membrane-bound structure analyzed by the transferred NOE experiments.

Structural information obtained from the chemical shifts is limited to local structural parameters like backbone dihedral angles. Thus the experimental methods for obtaining the information on side chain conformation and long-range order such as supra-secondary structures are necessary for the complete structure determination. For this purpose, dihedral

angles and distance measurements are useful (Fujiwara et al., 1998; Rienstra et al., 2002). The combined use of chemical shift analysis and structural parameter measurements would, therefore, facilitate the prompt determination of protein structures.

Acknowledgements

This research was partially supported by Grant-in-Aids for Scientific Research from the Ministry of Education and Science and by grants from the Japan New Energy and Industrial Technology Development Organization, and Yokohama City Collaboration of Regional Entities for the Advancement of Technological Excellence, Japan Science and Technology Corporation (JST) (H. A.). K.W. acknowledges the support by CREST, JST.

References

Astrof, N.S. and Griffin, R.G. (2002) *J. Magn. Reson.*, **158**, 157–163.

Balbach, J.J., Ishii, Y., Antzutkin, O.N., Leapman, R.D., Rizzo, N.W., Dyda, F., Reed, J. and Tycko, R. (2000a) *Biochemistry*, **39**, 13748–13759.

Balbach, J.J., Yang, J., Weliky, D.P., Steinbach, P.J., Tugarinov, V., Anglister, J. and Tycko, R. (2000b) *J. Biomol. NMR*, **16**, 313–327.

Baldus, M. (2002) *Progr. NMR Spectrosc.*, **41**, 1–47.

Baldus, M., Petkova, A.T., Herzfeld, J. and Griffin, R.G. (1998) *Mol. Phys.*, **95**, 1197–1207.

Bennett, A.E., Rienstra, C.M., Auger, M., Lakshmi, K.V. and Griffin, R.G. (1995) *J. Chem. Phys.*, **103**, 6951–6958.

Bennett, A,E., Rienstra, C.M., Griffiths, J.M., Zhen, W., Lansbury Jr., P.T. and Griffin, R.G. (1998) *J. Chem. Phys.*, **108**, 9463–9479.

Bevington, P.R. and Robinson, D.K. (1992) *Data Reduction and Error Analysis for the Physical Sciences*, WCB/McGraw-Hill, Boston, MA.

Caldarelli, S. and Emsley, L. (1998) *J. Magn. Reson.*, **130**, 233–237.

Castellani, F., van Rossum, B., Diehl, A., Schubert, M., Rehbein, K. and Oschkinat, H. (2002) *Nature*, **420**, 98–102.

Cavanagh, J., Fairbrother, W.J., Palmer III, A.G. and Skelton, N.J. (1996) *Protein NMR Spectroscopy*, Academic Press, San Diego, CA.

Cornell, W.D., Cieplak, P., Bayly, C.I., Gould, I.R., Merz Jr., K.M., Ferguson, D.M., Spellmeyer, D.C., Fox, T., Caldwell, J.W. and Kollman, P.A. (1995) *J. Am. Chem. Soc.*, **117**, 5179–5197.

Cornilescu, G., Delaglio, F. and Bax, A. (1999) *J. Biomol. NMR*, **13**, 289–302.

de Groot, H.J.M. (2000) *Curr. Opin. Struct. Biol.*, **10**, 593–600.

Detken, A., Hardy, E.H., Ernst, M., Kainosho, M., Kawakami, T., Aimoto, S. and Meier, B.H. (2001) *J. Biomol. NMR*, **20**, 203–221.

Egorova-Zachernyuk, T.A., Hollander, J., Fraser, N., Gast, P., Hoff, A.J., Cogdell, R., de Groot, H.J.M. and Baldus, M. (2001) *J. Biomol. NMR*, **19**, 243–253.

Foster, M.P., Wuttke, D.S., Clemens, K.R., Jahnke, W., Radhakrishnan, I., Tennant, L., Reymond, M., Chung. J. and Wright, P.E. (1998) *J. Biomol. NMR*, **12**, 51–71.

Fujiwara, T., Khandelwal, P. and Akutsu, H. (2000) *J. Magn. Reson.*, **145**, 73–83.

Fujiwara, T., Shimomura, T., Ohigashi, Y. and Akutsu, H. (1998) *J. Chem. Phys.*, **109**, 2380–2393.

Fujiwara, T., Sugase, K., Kainosho, M., Ono, A., Ono, A.(M.) and Akutsu, H. (1995) *J. Am. Chem. Soc.*, **117**, 11351–11352.

Griffin, R.G. (1998) *Nat. Struct. Biol.*, **5**, 508–512.

Hayashi, S. and Hayamizu, K. (1991) *Bull. Chem. Soc. Jpn.*, **64**, 685–687.

Higashijima, T., Burnier, J. and Ross, E.M. (1990) *J. Biol. Chem.*, **265**, 14176–14186.

Higashijima, T., Wakamatsu, K., Takemitsu, M., Fujino, M., Nakajima, T. and Miyazawa, T. (1983) *FEBS Lett.*, **152**, 227–230.

Hohwy, M., Rienstra, C.M. and Griffin, R.G. (2002) *J. Chem. Phys.*, **117**, 4973–4987.

Hohwy, M., Rienstra, C.M., Jaroniec, C.P. and Griffin, R.G. (1999) *J. Chem. Phys.*, **110**, 7983–7991.

Hong, M. (1999) *J. Biomol. NMR*, **15**, 1–14.

Hong, M. and Jakes, K. (1999) *J. Biomol. NMR*, **14**, 71–74.

Hughes, E. and Middleton, D.A. (2003) *J. Biol. Chem.*, **278**, 20835–20842.

Iwadate, M,. Asakura, T. and Williamson, M.P. (1999) *J. Biomol. NMR*, **13**, 199–211.

Kohno, T., Kusunoki, H., Sato, K. and Wakamatsu, K. (1998) *J. Biomol. NMR*, **12**, 109–121.

Kusunoki, H., Wakamatsu, K., Sato, K., Miyazawa, T. and Kohno, T. (1998) *Biochemistry*, **37**, 4782–4790.

LeMaster, D.M. and Kushlan, D.M. (1996) *J. Am. Chem. Soc.*, **118**, 9255–9264.

Lindberg, M., Jarvet, J. and Gräslund, A. (2001) *Biochemistry*, **40**, 3141–3149.

Luca, S., Filippov, D.V., van Boom, J.H., Oschkinat, H., de Groot, H.J.M. and Baldus, M. (2001) *J. Biomol. NMR*, **20**, 325–331.

Markley, J.L., Bax, A., Arata, Y., Hilbers, C.W., Kaptein, R., Sykes, B.D., Wright, P.E. and Wüthrich, K. (1998) *Pure Appl. Chem.*, **70**, 117–142.

Matsuki, Y., Akutsu, H. and Fujiwara, T. (2003) *J. Magn. Reson.*, **162**, 54–66.

Matsuzaki, K., Yoneyama, S., Murase, O. and Miyajima, K. (1996) *Biochemistry*, **35**, 8450–8456.

McDermott, A., Polenova, T., Bockmann, A., Zilm, K.W., Paulsen, E. K., Martin, R.W. and Montelione, G.T. (2000) *J. Biomol. NMR*, **16**, 209–219.

Metz, G., Wu, X. and Smith, S.O. (1994) *J. Magn. Reson. A*, **110**, 219–227.

Nomura, K., Takegoshi, K., Terao, T., Uchida, K. and Kainosho, M. (2000) *J. Biomol. NMR*, **17**, 111–123.

Pauli, J., Baldus, M., van Rossum, B., de Groot, H. and Oschkinat, H. (2001) *ChemBioChem*, **2**, 272–281.

Pauli, J., van Rossum, B., Förster, H., Huub, J.M., de Groot, H. and Oschkinat, H. (2000) *J. Magn. Reson.*, **143**, 411–416.

Petkova, A.T., Baldus, M., Belenky, M., Hong, M., Griffin, R.G. and Herzfeld, J. (2003) *J. Magn. Reson.*, **160**, 2–13.

Ponder, J.W. and Richards, F.M. (1987) *J. Comput. Chem.*, **8**, 1016–1024.

Rienstra, C.M., Hohwy, M., Hong, M. and Griffin, R.G. (2000) *J. Am. Chem. Soc.*, **122**, 10979–10990.

Rienstra, C.M., Tucker-Kellogg, L., Jaroniec, C.P., Hohwy, M., Reif, B., McMahon, M.T., Tidor, B., Lozano-Pérez, T. and Griffin, R.G. (2002) *Proc. Natl. Acad. Sci. USA*, **99**, 10260–10265.

Saito, H. and Ando, I. (1989) *Annu. Rep. NMR Spectrosc.*, **21**, 209–290.
Sayle, R.A. and Milner-White, E.J. (1995) *Trends Biochem. Sci*., **20**, 374–376.
Straus, S.K., Bremi, T. and Ernst, R.R. (1996) *Chem. Phys. Lett.*, **262**, 709–715.
Straus, S.K., Bremi, T. and Ernst, R.R. (1998) *J. Biomol. NMR*, **12**, 39–50.
Vold, R.R., Prosser, R.S. and Deese, A.J. (1997) *J. Biomol. NMR*, **9**, 329–335.
Wakamatsu, K., Okada, A., Miyazawa, T., Ohya, M. and Higashijima, T. (1992) *Biochemistry*, **31**, 5654–5660.
Whiles, J.A., Brasseur, R., Glover, K.J., Melacini, G., Komives, E.A. and Vold, R.R. (2001) *Biophys. J.*, **80**, 280–293.
Wishart, D.S. and Sykes, B.D. (1994) *Meth. Enzymol.*, **239**, 363–391.
Xu, X-P. and Case, D.A. (2001) *J. Biomol. NMR*, **21**, 321–333.
Xu, X-P. and Case, D.A. (2002) *Biopolymers*, **65**, 408–423.